FASTDEF: Fast defocus and astigmatism estimation for high-throughput transmission electron microscopy

J. Vargas [a,*], J. Otón [a], R. Marabini [b], S. Jonic [c], J.M. de la Rosa-Trevín [a], J.M. Carazo [a], C.O.S. Sorzano [a]

[a] Biocomputing Unit, Centro Nacional de Biotecnología-CSIC, C/ Darwin 3, 28049 Cantoblanco, Madrid, Spain
[b] Escuela Politécnica Superior, Univ. Autónoma de Madrid, 28049 Cantoblanco, Madrid, Spain
[c] IMPMC-UMR 7590, CNRS-Université Pierre et Marie Curie-IRD, 4 Place Jussieu, 75005 Paris, France

ABSTRACT

In this work we present a fast and automated algorithm for estimating the contrast transfer function (CTF) of a transmission electron microscope. The approach is very suitable for High Throughput work because: (a) it does not require any initial defocus estimation, (b) it is almost an order of magnitude faster than existing approaches, (c) it opens the way to well-defined extensions to the estimation of higher order aberrations, at the same time that provides defocus and astigmatism estimations comparable in accuracy to well established methods, such as Xmipp and CTFFIND3 approaches. The new algorithm is based on obtaining the wrapped modulating phase of the power spectra density pattern by the use of a quadrature filter. This phase is further unwrapped in order to obtain the continuous and smooth absolute phase map; then a Zernike polynomial fitting is performed and the defocus and astigmatism parameters are determined. While the method does not require an initial estimation of the defocus parameters or any non-linear optimization procedure, these approaches can be used if further refinement is desired. Results of the CTF estimation method are presented for standard negative stained images, cryo-electron microscopy images in the absence of carbon support, as well as micrographs with only ice. Additionally, we have also tested the proposed method with micrographs acquired from tilted and untilted samples, obtaining good results. The algorithm is freely available as a part of the Xmipp package [http://xmipp.cnb.csic.es].

© 2012 Elsevier Inc. All rights reserved.

1. Introduction

In transmission electron microscopy (TEM), a beam of electrons is transmitted through a specimen, magnified and focused onto a recording device, such as a CCD camera or a film. Because of the high resolution that can be achieved by TEMs, they are extensively used in structural biology to determine the structure of macromolecular complexes (van Heel et al., 2000; Frank, 2002; Henderson, 2004). However, an electron microscope, as any imaging device, distorts the ideal projections, modulating amplitudes and phases of the recorded electrons. Therefore, a critical step in the processing and analysis of EM images involves the estimation and correction of the distortions introduced by the TEM, which can be modeled in Fourier space by a linear transfer function known as the contrast transfer function (CTF).

Typically, the CTF is described analytically using a parametric form that takes into account defocus, astigmatism and spherical aberrations. These contrast transfer functions are estimated from the power spectrum density (PSD) that, in turn, is usually obtained by periodogram averaging (Avila-Sakar et al., 1994; Fernández et al., 1997) or parametric methods such as AR or ARMA (Velázquez-Muriel et al., 2003). In the past, different methods have been proposed to model and estimate the CTF using the PSD (Ludtke et al., 1999; Huang et al., 2003; Mindell and Grigorieff, 2003; Sander et al., 2003; Velázquez-Muriel et al., 2003; Mallick et al., 2005; Sorzano et al., 2007; Vulović et al., 2012). Typically, these methods try to fit the experimental CTF to an assumed parametric model (Ludtke et al., 1999; Huang et al., 2003; Mindell and Grigorieff, 2003; Sander et al., 2003; Velázquez-Muriel et al., 2003; Mallick et al., 2005; Sorzano et al., 2007). The fitting procedure consists in an iterative adjustment, where the discrepancy between simulated and experimental background-subtracted PSDs is minimized by a non-linear optimization that is dependent, for proper convergence, of the initial estimation. The fitting is either performed semiautomatically, with a graphical user interface (Ludtke et al., 1999), or automatically (Huang et al., 2003; Mindell and Grigorieff, 2003; Sander et al., 2003; Velázquez-Muriel et al., 2003; Mallick et al., 2005; Sorzano et al., 2007). There is a trade-off between the time required for the user to interact with the micrograph in a semiautomatic approach, and the larger processing time normally required by an automatic method. It is true that

* Corresponding author. Fax: +34 585 4506.
  E-mail address: jvargas@cnb.csic.es (J. Vargas).

modern microscopes can provide an estimation of the average defocus inside a range of about ±500 Å, but unless the work is performed under an integrated data management and data analysis framework, the user has to manually introduce these estimations one by one into the defocus estimation software. Note that this is an awkward and sensitive to errors process, especially if a large number of micrographs is going to be processed. Even more, there are cases in which an initial defocus estimation may be difficult to provide, as in the case of accurately retrieving the CTF parameters for small areas of a tilted micrograph. The examples above illustrate that there are clear situations in which a method which does not require an initial estimation is desirable. For completeness, it should be mentioned that, recently, Vulović et al. (2012) introduced a new approach that is not using an iterative non-linear optimization procedure. However, the application of this approach to more general cases than the ones presented in (Vulović et al., 2012) is still missing.

In this work, we present a novel approach to estimate the defocus and astigmatism parameters of a given micrograph. Our motivation is to help in the automation of the accurate processing of large quantities of data, including the individual treatment of multiple subareas of a micrograph. In this way, we present an approach that: (a) does not require any initial defocus estimation or even a parametric CTF model, (b) is almost an order of magnitude faster than existing approaches, (c) opens the way to well-defined extensions to the estimation of higher order aberrations, at the same time that provides a defocus and astigmatism estimations comparable in accuracy to well established existing methods such as Xmipp and CTFFIND3. Note that the estimation of higher order aberrations, as coma, is an important and open problem in single particle analysis. In (Glaeser et al., 2011), it is presented a deep analysis of the coma aberration influence in high-resolution Cryo-EM. As shown in (Glaeser et al., 2011), coma must be taken into consideration for resolutions lower than 8 Å, for typical TEMs and using accelerating voltages of 300 keV (indeed for 4 Å, it may cause the phases to be essentially random). Observe that for 200 keV, the resolution from which coma must be not neglected is of 18 Å. The method presented in this work is non-parametric and does not require a non-linear iterative optimization procedure, which makes it very fast. Moreover, even in combination with a posterior refinement method based on an iterative optimization, it is faster than currently available approaches. The proposed approach considers the CTF as a fringe pattern whose two-dimensional phase is modulated by a sine function and contains the information about the microscope aberrations. In order to estimate the phase map, we use a quadrature filter based on the Spiral Phase Transform (SPHT) (Larkin et al., 2001). This linear transformation approximately converts the sine of the phase map—the CTF signal—to the cosine of the phase map, which corresponds to the CTF quadrature signal. The wrapped phase map can be directly obtained from the arctangent of both signals in each pixel. This recovered wrapped phase map is limited to the range $(-\pi/2, \ \pi/2]$ rad. We unwrap this limited range phase and compute the absolute phase, that is not limited to a specific range. This absolute phase gives us the microscope aberrations, without assuming any parametric model in the CTF estimation process, where all aberrations and not only defocus, astigmatism and spherical aberrations, are contained. Finally, we fit the recovered absolute phase using Zernike polynomials and we obtain the third order Seidel aberrations, that include defocus and astigmatism. The estimated parameters can be further refined by any of the existing optimization-based methods, if desired.

The paper is organized as follows. In next section we present the theoretical basis of our method. In Section 3, we check the proposed approach with simulated and experimental PSDs and, finally, conclusions are drawn.

2. Theoretical foundations

In this section we: (1) introduce the image formation model based on the contrast transfer theory, in particular we describe the Contract Transfer Function (CTF) and its relationship to the power spectrum density (PSD), and (2) explain the proposed method to recover the CTF parameters.

2.1. Image formation model

We assume that the image formation model of an electron microscope is given by (Velázquez-Muriel et al., 2003; Sorzano et al., 2007)

$$p_{\exp}(\mathbf{r}) = h(\mathbf{r}) \cdot (p_{ideal}(\mathbf{r}) + p_{nb}(\mathbf{r})) + p_{na}(\mathbf{r}) \tag{1}$$

where $\mathbf{r} = [x, y]$ corresponds to the spatial coordinates, p_{ideal} is the ideal projection of the three-dimensional object being imaged, h is the Point Spread Function (PSF) of the microscope, $\cdot$ denotes the convolution operation and, finally, p_{nb} and p_{na} represent noise terms added before and after the convolution with the PSF. The corresponding PSD, using the image formation model presented in Expression (1), is calculated assuming that the energy of the noise before CTF is white and dominant over the energy of the imaged object. We refer to (Sorzano et al., 2007) to discuss this approximation). The mathematical expression of this PSD is given by

$$PSD(\mathbf{R}) = \sigma_{nb}^2 |H(\mathbf{R})|^2 + PSD_{na}(\mathbf{R}) \tag{2}$$

with, $\mathbf{R} = [R_x, R_y]$ the spatial frequency coordinates, σ_{nb}^2 a real number representing the noise power before CTF, $H(\mathbf{R})$ the CTF that corresponds to the Fourier Transform of the general PSF, $h(\mathbf{R})$, presented in Eq. (1). Finally, $PSD_{na}(\mathbf{R})$ refers to the PSD of the noise after CTF. The CTF of an electron microscope is given by the following expression (Ludtke et al., 1999; Huang et al., 2003; Mindell and Grigorieff, 2003; Sander et al., 2003; Velázquez-Muriel et al., 2003; Mallick et al., 2005; Sorzano et al., 2007; Vulović et al., 2012)

$$H(\mathbf{R}) = E(\mathbf{R})\left(A(\mathbf{R})\cos(\chi(\mathbf{R})) - \sqrt{1 - A^2(\mathbf{R})}\sin(\chi(\mathbf{R})) \right) \tag{3}$$

where $E(\mathbf{R})$ is a damping envelope and $A(\mathbf{R})$ corresponds to the fraction of electrons being scattered at each frequency—amplitude contrast. Note that $A(\mathbf{R})$ is usually considered as a constant and therefore, $A(\mathbf{R}) \cong A_0$. Taking into account the following trigonometric equality (MobileReference, 2009)

$$a\cos(x) + b\sin(x) = \sqrt{a^2 + b^2}\sin(x + \delta)$$
$$\delta = \arctan(a/b) + \begin{cases} 0 & b \geqslant 0 \\ \pi & b < 0 \end{cases} \tag{4}$$

where a, b, x and δ are generic real numbers, we can rewrite Eq. (3) as

$$H(\mathbf{R}) = E(\mathbf{R})\sin(\chi(\mathbf{R}) + \varphi)$$
$$\varphi = \arctan\left(\frac{A_0}{\sqrt{1 - A_0^2}}\right) + \pi \tag{5}$$

Note that Eqs. (3) and (5) are identical expressions written in different forms. We can see that the CTF is characterized by a contrast or amplitude modulating term $E(\mathbf{R})$, a modulating phase $\chi(\mathbf{R})$, that contains the microscope aberrations, and a phase-shift φ, that typically is small. Note that we normally measure the PSD and not the CTF, and the relationship between both is given in Expression (2). If we perform background suppression and mean subtraction to the PSD map, using for example the enhancing method presented in (Jonic et al., 2007), we have

$$PSD_m(\mathbf{R}) = \sigma_{nb}^2 E^2(\mathbf{R})\left(1/2 - \sin^2(\chi(\mathbf{R}) + \varphi)\right) \tag{6}$$

where $PSD_m(\mathbf{R})$ stands for the enhanced experimentally measured PSD.

2.2. Fast method for defocus and astigmatism estimation

We have divided this section into three subsections. In the first one, we introduce the quadrature operator based on the Spiral Phase Transform and the process to obtain a discontinuous wrapped phase. Then, we explain how to unwrap this phase in order to determine the smooth absolute phase. Finally, we show the process to compute the defocus and astigmatism parameters from the absolute phase by a Zernike polynomial fitting.

2.2.1. Quadrature operator and wrapped phase determination

Our objective in this subsection is to obtain the discontinuous wrapped phase and the contrast term from Expression (6). In Appendix A, we introduce a formal mathematical description of the wrapping operator. Intuitively, this operator transforms a continuous and smooth phase, with a dynamic range larger than 2π rad, into a discontinuous phase with a limited dynamic range inside the range $(-\pi/2, \pi/2]$ rad. Observe that Eq. (6) can be rewritten taking into account the trigonometric identity $\sin^2(\chi(\mathbf{R}) + \varphi) = [1 - \cos(2\chi(\mathbf{R}) + 2\varphi)]/2$ as

$$PSD_m(\mathbf{R}) = \sigma_{nb}^2 E^2(\mathbf{R}) \cos(2\chi(\mathbf{R}) + 2\varphi) \tag{7}$$

In general, a Quadrature operator transforms a trigonometric expression, as the one shown in Eq. (7), shifting the phase by $\pi/2$ rad (Larkin et al., 2001). Therefore, if we apply a Quadrature operator to Eq. (7), we obtain

$$Q[PSD_m] = \sigma_{nb}^2 E^2(\mathbf{R}) \sin(2\chi(\mathbf{R}) + 2\varphi) \tag{8}$$

where $Q[\cdot]$ is the Quadrature operator. Observe that if we compute the quadrature signal shown in Eq. (8), we can determine the wrapped modulating phase and the contrast term from Expressions (7) and (8) as

$$W[2\chi(\mathbf{R}) + 2\varphi] = \arctan\left(\frac{Q[PSD_m]}{PSD_m}\right)$$
$$\sigma_{nb}^2 E^2(\mathbf{R}) = \sqrt{(Q[PSD_m])^2 + (PSD_m)^2} \tag{9}$$

Note that the contrast term, or envelope map, $\sigma_{nb}^2 E^2(\mathbf{R})$, can be used as a quality map in order to obtain a processing mask, avoiding points with low signal to noise ration as

$$ROI(\mathbf{R}) = \frac{\sigma_{nb}^2 E^2(\mathbf{R})}{\text{MAX}\left[\sigma_{nb}^2 E^2(\mathbf{R})\right]} > m \tag{10}$$

with $ROI(\mathbf{R})$ the processing mask, MAX$[\cdot]$ an operator providing the maximum value of the map and m is a real number of about 0.1. It should be mentioned that the phase returned by an arctangent function in Eq. (9) will be wrapped if the dynamic range of this phase exceeds the range $(-\pi/2, \pi/2]$ rad, simply because of the limited range of the arctangent function.

A proper Quadrature operator is the Spiral Phase Transform (SPHT) (Larkin et al., 2001), converting a cosine signal into its quasi-quadrature signal, which is mathematically defined as (Larkin et al., 2001)

$$SPHT[\cdot] = FT^{-1}\left[\left(\frac{\hat{x} + i\hat{y}}{\sqrt{\hat{x}^2 + \hat{y}^2}}\right)FT[\cdot]\right] \tag{11}$$

where $SPHT[\cdot]$ is the Spiral Phase Transform operator, $(\hat{x}, \hat{y})$ are the transformed spatial coordinates, FT and FT^{-1} means 2D Fourier Transform and 2D Inverse Fourier Transform and $i = \sqrt{-1}$. Observe that the SPHT introduced in Eq. (11) corresponds to a 2D Hilbert transform (Larkin et al., 2001). If we now apply the Spiral Phase

Transform operator to PSD_m as presented in Eq. (7), we obtain (Larkin et al., 2001)

$$SPHT[PSD_m(\mathbf{R})] = i\exp(iD(\mathbf{R}))\sigma_{nb}^2 E(\mathbf{R})^2 \sin(2\chi(\mathbf{R}) + 2\varphi) \tag{12}$$

Observe that $SPHT[PSD_m(\mathbf{R})]$ corresponds to $Q[PSD_m]$ multiplied by an additional phase given by $i\exp(iD(\mathbf{R}))$. In Eq. (12), $D(\mathbf{R})$ is normally referred as the phase direction map, and corresponds to the subtended angle of the phase gradient vector with respect to the R_x-axis. In our case, where the phase is mainly composed by defocus aberration, we can calculate the direction map by (see Appendices B and C, for further information)

$$D(\mathbf{R}) \cong \arctan\left(\frac{R_y}{R_x}\right) \tag{13}$$

The quadrature signal of PSD_m is given from Expression (8) and (12) by

$$Q[PSD_m(\mathbf{R})] = \sigma_{nb}^2 E^2(\mathbf{R}) \sin(2\chi(\mathbf{R}) + 2\varphi)$$
$$= -i\exp(-iD(\mathbf{R}))SPHT[PSD_m(\mathbf{R})] \tag{14}$$

Using the quadrature signal of PSD_m, shown in Eq. (14), and the PSD_m, we obtain the wrapped phase and the contrast term from Eq. (9).

2.2.2. Phase unwrapping process

Phase unwrapping is an important image-processing technique that has been applied in many fields such as magnetic resonance imaging (MRI), synthetic aperture radar interferometry (InSAR), and optical interferometry. Many accurate methods for phase unwrapping have been proposed in the literature (Goldstein et al., 1988; Ghihlia and Romero, 1994; Flynn, 1997; Navarro et al., 2012). Typically, the output of many processes is not the desired absolute phase but a wrapped phase that corresponds to the absolute phase modulo 2π, i.e.

$$W[2\chi(\mathbf{R}) + 2\varphi] = 2\chi(\mathbf{R}) + 2\varphi - 2\pi k \tag{15}$$

where k is an integer. The aim of the phase unwrapping process is to obtain the absolute phase $2\chi(\mathbf{R}) + 2\varphi$ through the wrapped phase $W[2\chi(\mathbf{R}) + 2\varphi]$. Obviously, the problem is ill conditioned, as multiple values of the absolute phase can be obtained by one wrapped phase with different ks. Therefore, phase unwrapping is an inverse problem with no unique solution. To find a unique solution additional constrains are needed. In this way, almost all phase unwrapping methods imposes continuity in the absolute phase and, furthermore, assume that the absolute value of the absolute phase difference between adjacent pixels is less than π.

In this work, we have used the method presented in (Navarro et al., 2012), that corresponds to a fast unwrapping two-dimensional algorithm based on a linear recursive filter. This recursive filter can be seen as composed by two terms: a predictor, that is an estimation based on previously unwrapped values, and a corrector, that takes into account wrapped input data to correct the current estimation. This method is robust to noise because its smoothing capabilities (Navarro et al., 2012). Therefore, using this unwrapping approach we can compute the absolute phase map, that it is given by

$$2\chi(\mathbf{R}) + 2\varphi = W[2\chi(\mathbf{R}) + 2\varphi] + 2\pi k \tag{16}$$

where $W[2\chi(\mathbf{R}) + 2\varphi]$ has been obtained from Eq. (9) and the ks from the unwrapping process.

2.2.3. Zernike fitting. Determination of the defocus and astigmatism parameters

Once we have computed the absolute phase map, we can perform a Zernike polynomials fitting. The Zernike polynomials correspond to a complete polynomial basis that is orthonormal in the

unit disk (Wyant and Creath, 1992). These polynomials are extensively used in optics, especially in the interpretation of optical test results, because they have the same form as the types of aberrations often observed in optical systems (Wyant and Creath, 1992). In Table 1, we give the mathematical expressions and names of the first nine Zernike polynomials. Taking into account that the Zernike polynomials are a complete polynomial basis, the absolute phase can be expressed as a linear combination of these polynomials as

$$2\chi(\mathbf{R}) + 2\varphi = \sum_j Z_j ZPol_j(\mathbf{R}) \tag{17}$$

where Z_j are the different Zernike coefficients, whose values are obtained fitting the absolute phase with the Zernike polynomials. In Appendix D, we give the mathematical expressions of the Zernike polynomials $ZPol_j(\mathbf{R})$. Observe that we can obtain the Zernike coefficients directly from Eq. (17) by a simple linear least-squares as

$$q = M \cdot Z \tag{18}$$

where q is a column vector of size $N_x N_y \times 1$, with N_x and N_y the number of columns and rows of the absolute phase image, whose elements are taken columnwise from $2\chi(\mathbf{R}) + 2\varphi$. Additionally, Z is a column vector of dimension N composed by the Zernike coefficients that corresponds to the number of Zernike polynomials used. Finally, M is a matrix of size $N_x N_y \times N$, where the nth column is taken columnwise from the nth Zernike polynomial. The Zernike polynomials can be directly obtained by

$$Z = M^+ q \tag{19}$$

with M^+ the Moore–Penrose pseudoinverse of M that is given by $M^+ = (M^T M)^{-1} M^T$.

The third-order wavefront aberration coefficients, most commonly known as Seidel aberrations, can be obtained directly from the Zernike polynomials coefficients. Seidel aberrations appear in any image formation system when the paraxial approximation is not sufficient for an accurate description of the system. The paraxial approximation establishes that $\sin(\phi) \cong \phi$ in the refraction law, with ϕ the refraction angle. This approximation considers that lenses are perfect and/or the refraction angle is very small. If we include quadratic and cubic terms in the refraction law, then third-order aberrations appear, resulting from imperfections in real lenses. The five Seidel aberrations are: spherical aberration, coma, astigmatism, curvature of field and distortion (Born and Wolf, 1975). Observe that the defocus does not appear as a Seidel aberration. This is because Seidel aberrations only care about distortions caused by imperfections in the lenses and/or large refraction angles. On the other hand, defocus only depends on the position of the observation plane, so a perfect imaging system with perfectly parallel incoming rays with respect to the optical axis will have defocus if the imaging plane is not in focus. In

Table 1
Mathematical expressions and names of the first nine Zernike polynomials. The indexes n, m, j, correspond to the way to refer the Zernike polynomials and are discussed in Appendix D.

Coefficient	Name	n	m	j	Polynomial
Z_0	Piston	0	0	0	1
Z_1	x-tilt	1	1	1	$r\cos\alpha$
Z_2	y-tilt	1	1	2	$r\sin\alpha$
Z_3	Defocus	1	0	3	$2r^2 - 1$
Z_4	x-astig. & defocus	2	2	4	$r^2\cos(2\alpha)$
Z_5	y-astig. & defocus	2	1	5	$r^2\sin(2\alpha)$
Z_6	x-coma & tilt	2	1	6	$(3r^2 - 2)r\cos(\alpha)$
Z_7	y-coma & tilt	2	1	7	$(3r^2 - 2)r\sin(\alpha)$
Z_8	Spherical & defocus	2	0	8	$6r^4 - 6r^2 + 1$

Table 2
Third-order Seidel aberrations coefficients obtained from Zernike polynomials coefficients.

Piston	$Z_0 - Z_3 + Z_8$
Tilt	$r\sqrt{(Z_1 - 2Z_6)^2 + (Z_2 - 2Z_7)^2}\cos\left[\theta - \arctan\left(\frac{((Z_2 - 2Z_7))}{(Z_1 - 2Z_6)}\right)\right]$
Defocus	$r^2 2(Z_3 - 6Z_8) \pm \sqrt{Z_4^2 + Z_5^2}$
Astigmatism	$\pm 2r^2 \sqrt{Z_4^2 + Z_5^2}\cos^2\left[\alpha - \frac{1}{2}\arctan\left(\frac{Z_5}{Z_4}\right)\right]$
Coma	$3r^3 \sqrt{Z_6^2 + Z_7^2}\cos\left[\alpha - \arctan\left(\frac{Z_7}{Z_6}\right)\right]$
Spherical	$6r^4 Z_8$

electron microscopy, we care especially about defocus, spherical and astigmatism aberrations. First order wavefront properties and third-order aberrations coefficients can be obtained from Zernike polynomials coefficients. Using the first nine Zernike terms, Z_0 to Z_8 shown in Table 1, the relationships are given in Table 2. Note that defocus has the sign chosen to minimize the magnitude of the coefficient, and astigmatism uses the sign opposite to the one chosen for defocus. For angle calculations in Table 2, note that if the denominators are less than 0, then the angles correspond to the angle value plus π rad (Wyant and Creath, 1992).

The phase value χ introduced in Expression (5) is given, for a typical electron microscope, as

$$\chi(\mathbf{R}) = \pi\lambda_{re}\left(-\Delta f(\mathbf{R})|\mathbf{R}|^2 + \frac{C_s|\mathbf{R}|^4\lambda_{re}^2}{2}\right)$$
$$\Delta f(\mathbf{R}) = (\Delta f_{avg} + \Delta f_{diff}\cos(2(\alpha - \alpha'))) \tag{20}$$
$$\Delta f_{avg} = \frac{\Delta f_u + \Delta f_v}{2}, \quad \Delta f_{diff} = \frac{\Delta f_u - \Delta f_v}{2}$$

with, λ_{re} the wavelength of electrons in the microscope, C_s the spherical aberration of the microscope lens and α' is the astigmatism angle. If we sum the defocus, astigmatism and spherical Seidel aberrations given in Table 2, we have that

$$\chi(\mathbf{R}) = -\frac{1}{2}\{T_s^2|\mathbf{R}|^2\left[2(Z_3 - 6Z_8) \mp \sqrt{Z_4^2 + Z_5^2}\cos(2(\alpha - \tilde{\alpha}))\right]$$
$$+ 6|\mathbf{R}|^4 T_s^4 Z_8\} \tag{21}$$

where T_s is the sampling rate. Comparing Expression (20) and (21) we can obtain the CTF parameters as

$$\Delta f_{avg} = \frac{T_s^2(Z_3 - 6Z_8)}{\pi\lambda_{re}}$$
$$\Delta f_{diff} = \frac{T_s^2\sqrt{Z_4^2 + Z_5^2}}{\pi\lambda_{re}} \tag{22}$$
$$C_s = \frac{3T_s^4 Z_8}{\pi\lambda_{re}^3}$$

and the astigmatism angle is given by

$$\alpha' = \begin{cases} \tilde{\alpha} & + \text{ sign in Eq. (21)} \\ \tilde{\alpha} + \pi & - \text{ sign in Eq. (21)} \end{cases} \tag{23}$$

Note that the initial estimation of the CTF parameters can be further refined by any of the CTF estimation methods based on a non-linear optimization. In this work, we have used the method presented in (Sorzano et al., 2007) for further refinement. In Fig. 1, we show a diagram where we summarize the different processing steps.

3. Results

The new algorithm has been implemented in the Xmipp package (http://xmipp.cnb.csic.es, Sorzano et al., 2004). In order to check for the accuracy of the proposed method, the first level of testing has involved image simulations. Upon successful evaluation, several experimental datasets have been processed, including cryo-electron microscopy images in the absence of carbon support,
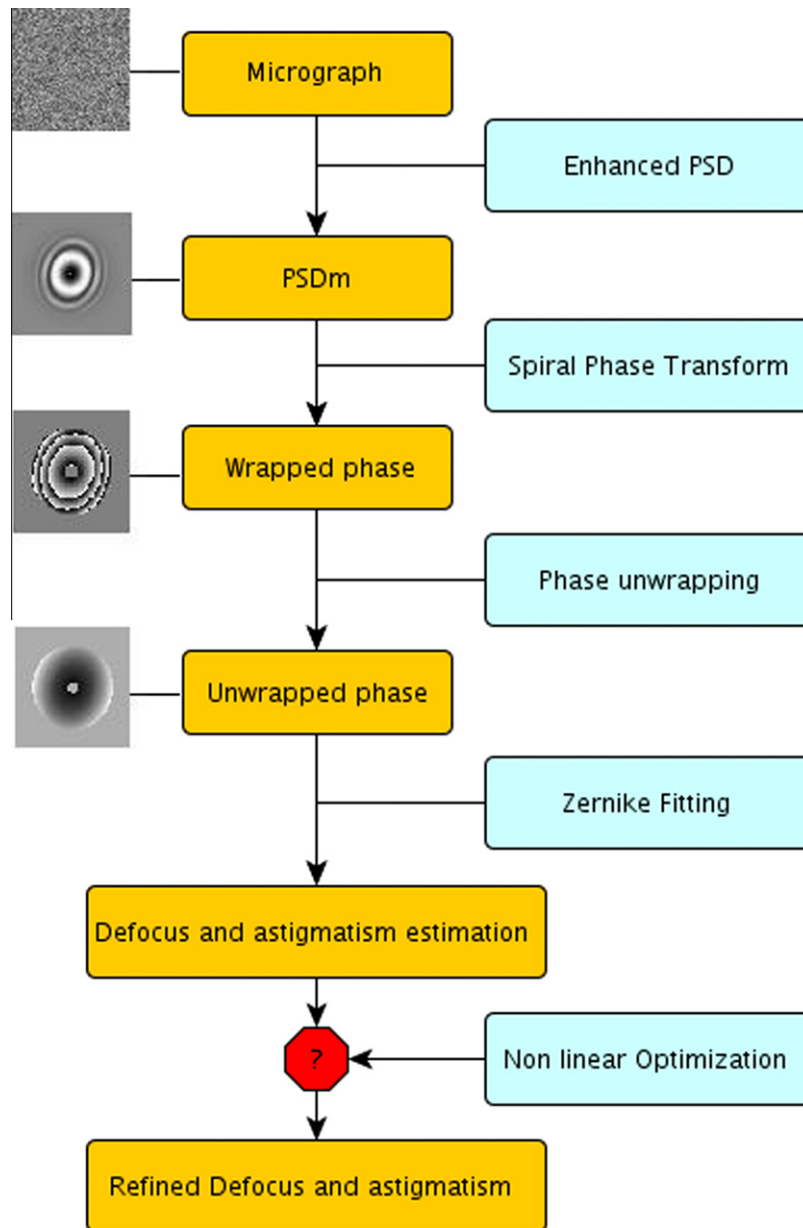
Fig.1. Diagram that shows the different processing steps used by the proposed CTF estimation method.

tilted and untilted standard negative stained images as well as micrographs containing only ice.

3.1. Simulations

In order to show the performance of the proposed method, we have tested it using a set of simulated micrographs from which we have obtained the PSDs. In the simulations, we have compared the results obtained by the method presented in this study—FASTDEF method—with the results obtained by CTFFIND3 (Mindell and Grigorieff, 2003) and Xmipp (Sorzano et al., 2007) approaches. Additionally, we also show the results obtained when we refine the results retrieved by the FASTDEF method with the optimization method presented in (Sorzano et al., 2007). This method will be denoted as FASTDEF + Xmipp approach. The comparison between the different CTF estimating techniques is made in terms of accuracy and processing speed. In order to quantify the accuracy of the different results, we compute the Euclidean distance between the true and estimated Δf_u and Δf_v parameters. We have used five sim-

ulated micrographs using Xmipp package of size 1024×1024 px with a pixel size of 3.6 Å per pixel. No particle was present in the simulated micrographs. In this numerical experiment we know exactly the underlying PSD and, therefore, we can obtain the accuracy of the estimated PSDs comparing them with the ground truth values. Note that Xmipp, FASTDEF and CTFFIND3 obtain the PSD from the micrographs in the same way, by periodogram averaging using averaging windows of 256×256 px. In Fig. 2, we show the simulated PSDs used to test the different algorithms. As can be seen from Fig. 2, we use a heterogeneous group, with some PSDs with small and large defocus values and with or without astigmatism. For the PSD shown in Fig. 2(a), we present in Fig. 3, its obtained wrapped phase (a), the unwrapped phase (b), the fitted phase by Zernike polynomials (c) and the cosine of the fitted phase by Zernike polynomials (d). As can be seen from Fig. 3, the wrapped phase (Fig. 3(a)) has a set of discontinuities that disappear in the unwrapped phase map. Additionally, the Zernike fitting reduces possible image artifacts that can appear in the phase map. In Fig. 4, we represent the obtained values for the first eight Zernike
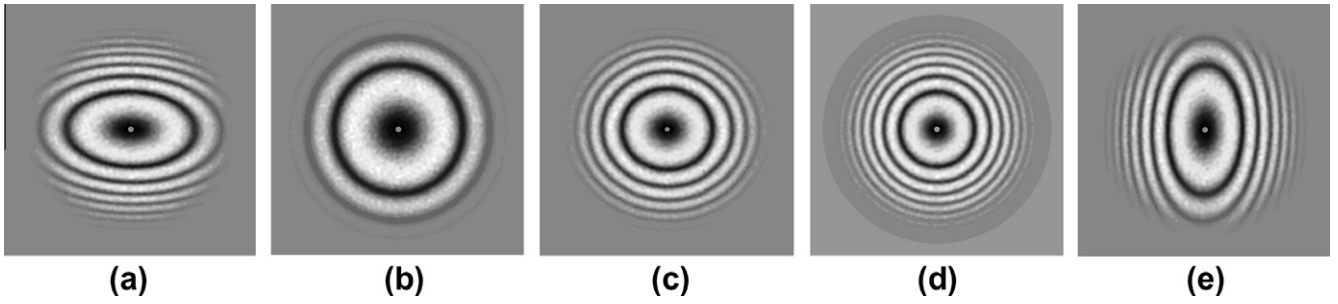
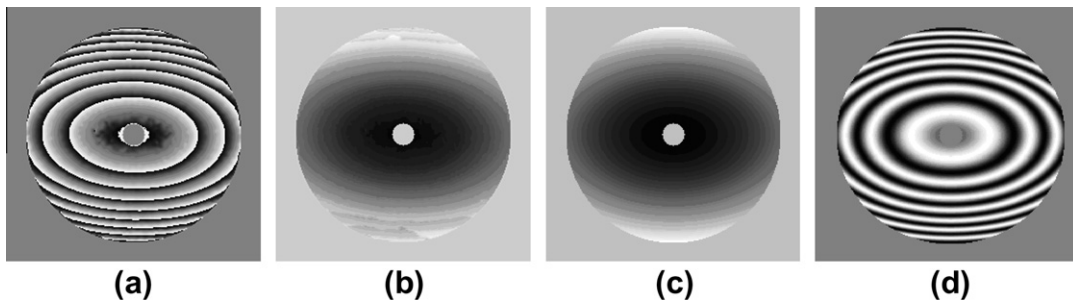**Fig.2.** The five simulated PSDs used in the simulation section.

Fig.3. Wrapped phase (a), unwrapped phase (b), fitted phase by Zernike polynomials (c) and cosine of the fitted phase by Zernike polynomials (d) obtained from the PSD shown in Fig. 2(a).
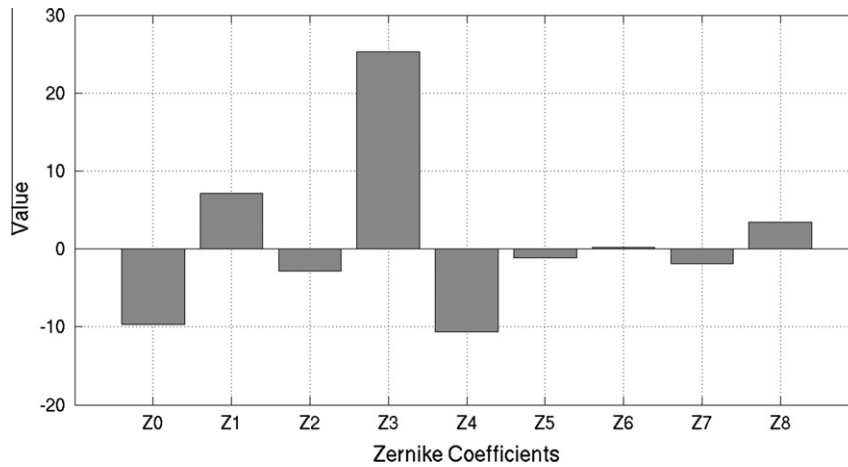

Fig.4. Obtained values of the first eight Zernike coefficients for the simulated PSD shown in Fig. 2(a).

Table 3
Ground truth CTF parameters and results obtained by FASTDEF ($\Delta f^{(1)}$), FASTDEF + Xmipp ($\Delta f^{(2)}$), Xmipp ($\Delta f^{(3)}$) and CTFFIND3 ($\Delta f^{(4)}$) in Angstrom units, when the simulated PSDs shown in Fig. 2 are processed.

	$\Delta f_{u,\,th}$	$\Delta f_{v,\,th}$	$\Delta f_u^{(1)}$	$\Delta f_v^{(1)}$	$\Delta f_u^{(2)}$	$\Delta f_v^{(2)}$	$\Delta f_u^{(3)}$	$\Delta f_v^{(3)}$	$\Delta f_u^{(4)}$	$\Delta f_v^{(4)}$
Fig. 3(a)	30000	10000	27810	10047	29881	9909	29883	9907	29973	9893
Fig. 3(b)	10000	10000	10481	10456	9977	9971	9956	9967	9773	9795
Fig. 3(c)	25000	20000	24747	20115	25015	19941	25033	19940	24871	20048
Fig. 3(d)	30000	30000	28141	27809	29897	29887	29897	29886	29810	29851
Fig. 3(e)	30000	10000	29906	9976	29874	9903	29879	9905	29960	9845

coefficients, where the largest Zernike coefficients correspond to Z_3 and Z_4 coefficients, which, according to Table 1, correspond to defocus and x-astigmatism & defocus aberrations. Additionally, we can see from Fig. 4 that the Zernike fitting provides us addi-

tional information about important higher order microscope aberrations, such as coma (that corresponds to Z_6 and Z_7 values in Fig. 4) which are not accessible using typical parametric methods, such as Xmipp or CTFFIND3. In Table 3 we present the ground truth

Table 4
Relative errors obtained by FASTDEF ($\varepsilon_r^{(1)}$), FASTDEF + Xmipp ($\varepsilon_r^{(2)}$), Xmipp ($\varepsilon_r^{(3)}$) and CTFFIND3 ($\varepsilon_r^{(4)}$) in Angstrom units, when are processed the simulated PSDs shown in Fig. 2.

	$\varepsilon_r^{(1)}$ (%)	$\varepsilon_r^{(2)}$ (%)	$\varepsilon_r^{(3)}$ (%)	$\varepsilon_r^{(4)}$ (%)
Fig. 3(a)	6.9	0.47	0.47	0.35
Fig. 3(b)	4.7	0.26	0.39	2.16
Fig. 3(c)	0.87	0.19	0.21	0.43
Fig. 3(d)	6.8	0.36	0.36	0.57
Fig. 3(e)	0.31	0.50	0.49	0.51

CTF parameters and the results obtained by the different methods. In order to compare the different results, we present in Table 4 the relative errors obtained by the different approaches. Additionally, The processing times required to process the five PSDs on a 2.4 GHz laptop are 75, 171, 855 and 1030 s for FASTDEF, FAST-DEF + Xmipp (refined FASTDEF results), Xmipp, and CTFFIND3, respectively. These processing times have been obtained using a defocus search range of [0.5, 10] μm for both the Xmipp and CTF-FIND3 methods. Finally, in Fig. 5, we show the ground-truth and estimated PSDs for the five images shown in Fig. 2 when using the FASTDEF method. As can be seen from Fig. 5, there is a good agreement between the simulated and retrieved Thon rings in all cases.

From the results presented above, we can see that both FAST-DEF and FASTDEF + Xmipp are quite fast ways to obtain the CTF parameters. Indeed, compared to Xmipp and CTFFIND3, FASTDEF is 14 and 11 times faster, while FASTDEF + Xmipp is 7.8 and 8.0 times faster, respectively, always for similarly accurate results.

3.2. Experimental results

We have also tested the proposed method with experimental PSDs. Three datasets of experimental images, represented as BPV, CL and P53, are used. In the first case, the specimen was deposited on holey grids and cryo-preserved. The images correspond, therefore, to typical cryo-microscopy images with no carbon support. The second case corresponds to negative staining performed with 0.75% uranyl formiate, over glow discharged Quantifoil Formvar/ Carbon grids. Finally, in the third case, negative staining was performed with uranyl formiate in carbon sandwich technique over Quantifoil grids. The dataset BPV (Wolf et al., 2010) consists of images of Bovine Papillomavirus and have a sampling rate of 1.237 Å per pixel and the micrographs have a size of 9216 × 9441 px. On the other hand, the CL dataset contains images of *Escherichia Coli* DNA Polymerase III clamp loader with a notice-able astigmatism, that were digitized with a pixel size of 3.5 Å. The *E. coli* Gama(370)4-Psi-Chi, is a 197 kDa complex, composed by four copies of a truncated form of the protein Gamma (residues 1–370), one unit of Psi and one unit of Chi. In this case, the micrograph size is 3212 × 2539 px. The P53 dataset consists in a deletion
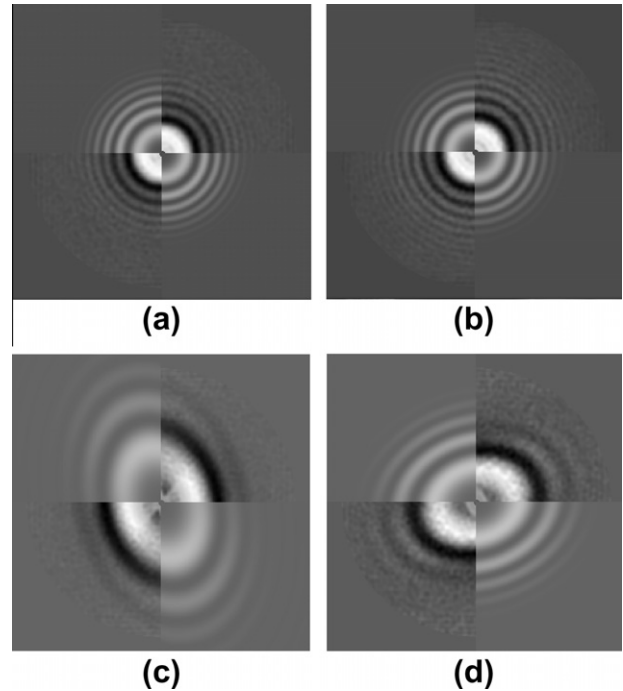

Fig.6. Enhanced experimental and fitted PSDs using the FASTDEF method for two micro graphs of the BPV dataset (a), (b) and two micrographs of the CL dataset (c), (d).

mutant of human p53, lacking its 33 C-terminal residues (NTC, p531-360) and with four stabilizing mutations in the core domain (M133L/V203A/N239Y/N268D) (Melero et al., 2011). Images are recorded in a 4k × 4k CCD camera at a magnification of a 64305× corresponding to a 2.1 Å pixel size.

In Fig. 6, we show the enhanced experimental PSD and the fitted theoretical PSD using the FASTDEF method for two micrographs, one from the BPV and CL groups, although the method was suc-cessfully applied to all the micrographs in the datasets. We use the method presented in (Jonic et al., 2007) for enhancing the PSDs. Note that for both datasets, FASTDEF, Xmipp and CTFFIND3 obtain the PSD from the micrographs by periodogram averaging using averaging windows of 256 × 256 px. In order to estimate the CTF parameters, we only need to provide to the proposed algorithm the enhanced experimental PSD estimated by periodogram averag-ing, the microscope voltage and the micrograph sampling rate. The BPV dataset is composed of 49 micrographs of good quality, while the CL one has 24 micrographs with large astigmatism. The data from BPV was acquired using a FEI Tecnai F30 electron microscope (300 kV) with nominal magnification of 59000×. The spherical aberration is 2.26 in mm. On the other hand, the data from the CL dataset was obtained from a JEOL JEM-1011 electron micro-
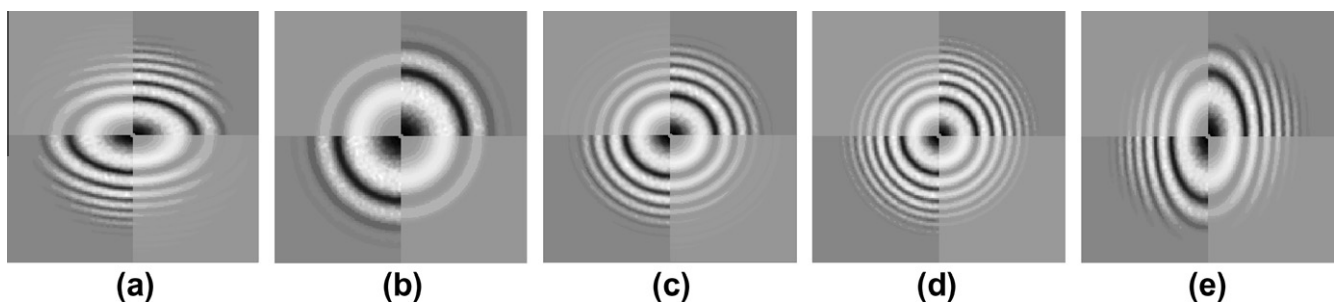

Fig.5. Simulated and obtained PSDs for the five images shown in Fig. 2.

scope (100 kV) with nominal magnification of 60000×. The spherical aberration is 5.6 mm. In Fig. 7, we show a plot of the obtained defocus results for the BPV and CL datasets when we use the FAST-DEF (dashed line with brown squares), FASTDEF + Xmipp (solid black line with dark circles), Xmipp (solid black line with white circles) and CTFFIND3 (dotted black line with bright circles) methods. For comparison purposes, we show in Fig. 8 the difference between the defocuses obtained by each method and the average defocus values, computed using the results from all the approaches (FAST-DEF, FASTDEF + Xmipp, Xmipp and CTFFIND3) . As can be seen from Figs. 7 and 8, there is good agreement between the different defocus results. In order to quantify the accuracy and precision of the computed defocus results acquired by FASTDEF and FAST-DEF + Xmipp approaches, we have obtained the mean and standard deviation (*std*) between the average defocuses retrieved by these methods and Xmipp and CTFFIND3 approaches. In Table 5, we show the obtained results. As can be seen from Table 5, the differences in the defocus average between the FASTDEF and FAST-DEF + Xmipp methods with respect to Xmipp and CTFFIND3 are not significant for the BPV dataset. In the case of the CL dataset, we see that there is also a good agreement between the results obtained by FASTDEF and FASTDEF + Xmipp with respect to Xmipp method. Observe that the CTF determination of these micrographs

is challenging because the large astigmatism and low contrast Thon rings that have the PSDs of this dataset. The computation times required to process the two different datasets are 967 s, 2243 s, 11239 s, 8240 s for the BPV and 251 s, 1355 s, 5952 s, 5623 s for the CL dataset when processing using the FASTDEF, FASTDEF + Xmipp, Xmipp and CTFFIND3 methods, respectively. Observe that the BPV and CL datasets are composed by 49 and 24 micrographs. In Table 6, we show the mean processing time and per micrograph and standard deviation for each dataset, when we process them using the different methods. Note that for the case of FASTDEF, FASTDEF + Xmipp and Xmipp, the estimation of the PSD by periodogram averaging takes approximately seven and two seconds per micrograph for the BPV and CL datasets, respectively. These times are included in the processing times reported above and have been obtained using a defocus search range of [0.5, 10] μm for both the Xmipp and CTFFIND3 methods. We use such a large defocus range because, in our experience, many users do not always provide an initial accurate estimation of the defocus average values and they prefer to select a large defocus search range, especially when they process a large group of micrographs with different CTFs. Note that in the case of the Xmipp package, the CTF estimation program uses as default a defocus search range of [0.5, 10] μm. As can be seen from these results, the FASTDEF and
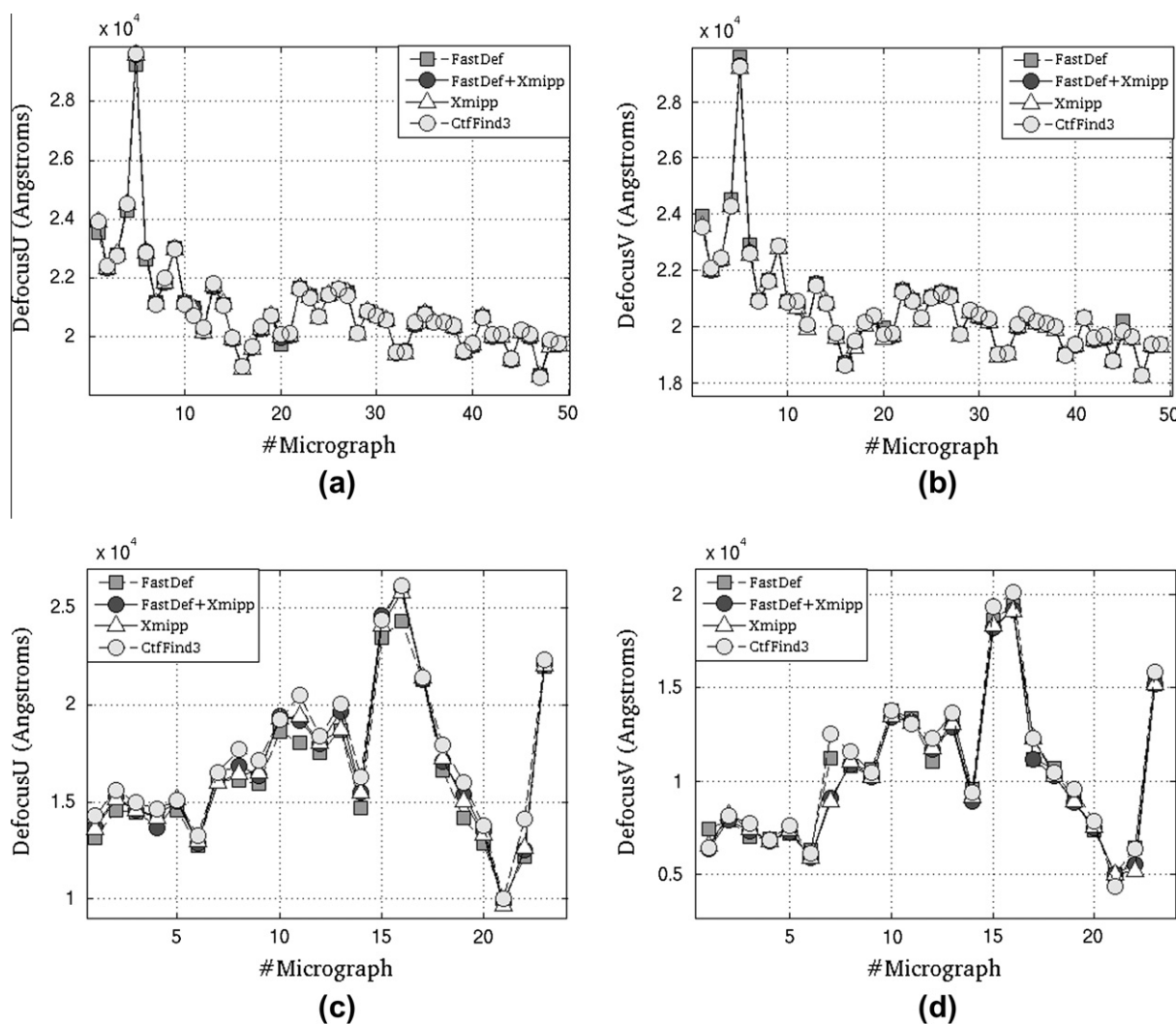

Fig.7. Defocus results for the different micrographs obtained by the FASTDEF (dashed line with brown squares), FASTDEF + Xmipp (solid black line with dark circles), Xmipp (solid black line with white circles) and CTFFIND3 (dotted black line with bright circles) methods for the BPV (a), (b) and CL datasets (c), (d).
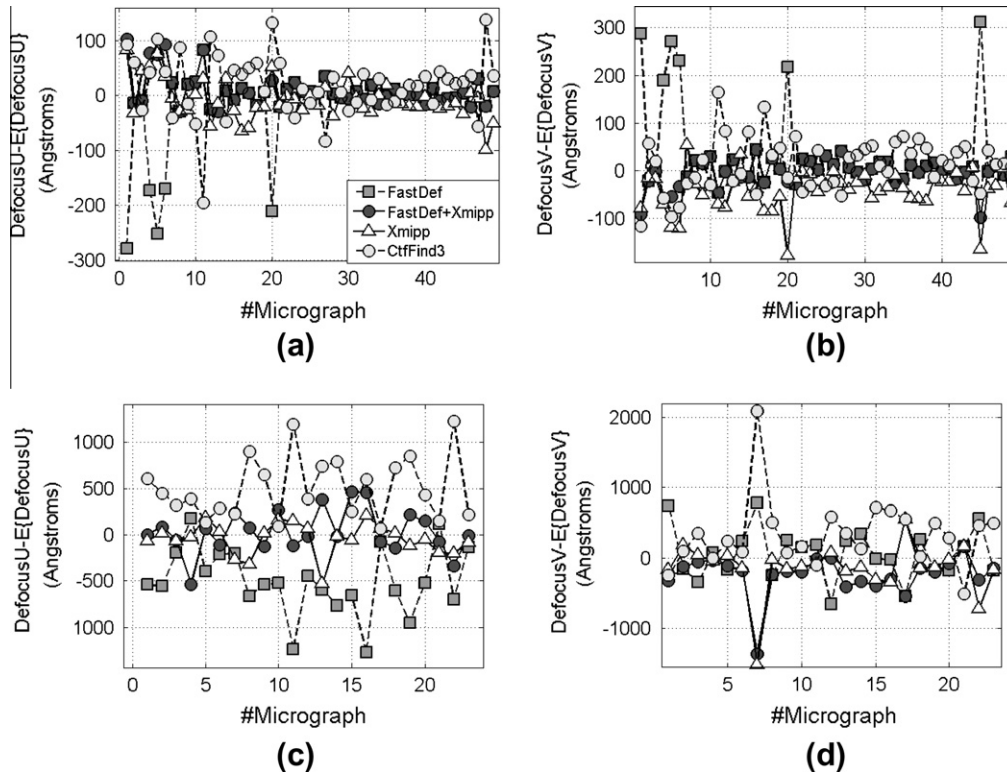
Fig.8. Difference between the defocus results obtained by the FASTDEF (dashed line with brown squares), FASTDEF + Xmipp (solid black line with dark circles), Xmipp (solid black line with white circles) and CTFFIND3 (dotted black line with bright circles) methods and the average defocus values computed using the results from all the approaches, for the BPV (a), (b) and CL datasets (c), (d).

Table 5
Mean and standard deviation obtained between the average defocuses retrieved by the FASTDEF and FASTDEF + Xmipp methods and Xmipp and CTFFIND3 approaches, for the BPV and CL datasets.

	Xmipp (Å)		CTFFIND3 (Å)	
	Mean	Std	Mean	Std
BPV				
FASTDEF	32	42	−8.0	53
FASTDEF + Xmipp	28	27	−12	46
CL				
FASTDEF	−180	250	−490	322
FASTDEF + Xmipp	−7.0	190	−420	221

Table 6
Processing times per micrograph and standard deviations obtained when we process the BPV and CL datasets using the FASTDEF and FASTDEF + Xmipp, Xmipp and CTFFIND3 methods.

	Time (s)	Std (s)
BPV		
FASTDEF	20	1.2
FASTDEF + Xmipp	46	6.8
Xmipp	229	70
CTFFIND3	168	42
CL		
FASTDEF	11	2.1
FASTDEF + Xmipp	56	21
Xmipp	248	34
CTFFIND3	234	3.6

Table 7
Computation times obtained when it is processed one micrograph of the BPV dataset for different periodogram averaging window sizes and using FASTDEF, FASTDEF + Xmipp, Xmipp and CTFFIND3 methods.

	Size (px)				
	200	250	300	350	400
FASTDEF (s)	15	18	22	23	25
FASTDEF + Xmipp (s)	26	39	43	58	66
Xmipp (s)	134	165	206	302	726
CTFFIND3 (s)	126	223	400	580	785

have similar accuracy than these approaches. We have also studied the dependency of the different methods with respect to the periodogram averaging window size. We have obtained, for one micrograph of the BPV dataset, the CTF parameters for different averaging window sizes. The results are presented in Table 7. As can be seen from Table 7, the processing time scales approximately linearly with respect to the averaging window size for the FASTDEF and FASTDEF + Xmipp methods. Note, that this is not true for the Xmipp and CTFFIND3 approaches. Additionally, the standard deviation of the mean defocus values for the averaging window sizes shown in Table 7 are 272, 6, 28 and 20 Å when we process using FASTDEF, FASTDEF + Xmipp, Xmipp and CTFFIND3 methods.

The defocus average parameter can be considered as the distance between the sample and the focal plane of the objective lens (Mindell and Grigorieff, 2003). Therefore, tilt information can be obtained from the local defocus variation along a micrograph. In this way, we can divide an image in multiple subimages and calculate for each one of them its CTF parameters. Note that, in this case, the defocus estimation provided by the microscope is not accurate because it consists on an average of a locally varying magnitude.

FASTDEF + Xmipp methods are approximately ten and five times faster than the CTFFIND3 and Xmipp methods, respectively, and

Table 8
Fitted plane parameters by the locally retrieved defocus average values using FASTDEF, FASTDEF + Xmipp, Xmipp and CTFFIND3 methods for the tilted and untilted micrographs of P53 dataset.

	Untilted$_1$ × 10^3 (Å)	Tilted$_1$ × 10^3 (Å)
FASTDEF	$(-3.63x - 5.19y) \cdot 10^{-5} + 8.03$	$(-1.26x - 6.83y) \cdot 10^{-4} + 9.72$
FASTDEF + Xmipp	$(-3.72x - 4.93y) \cdot 10^{-5} + 8.03$	$(-1.27x - 6.74y) \cdot 10^{-4} + 9.71$
Xmipp	$(-4.18x - 5.23y) \cdot 10^{-5} + 8.24$	$(-1.12x - 6.29y) \cdot 10^{-4} + 9.67$
CTFFIND3	$(-4.09x - 4.65y) \cdot 10^{-5} + 8.28$	$(-1.26x - 6.29y) \cdot 10^{-4} + 9.75$
	Untilted$_2$ × 10^3 (Å)	Tilted$_2$ × 10^3 (Å)
FASTDEF	$(-6.32x - 7.35y) \cdot 10^{-5} + 8.70$	$(-1.32x - 6.60y) \cdot 10^{-4} + 11.2$
FASTDEF + Xmipp	$(-5.71x - 6.49y) \cdot 10^{-5} + 8.67$	$(-1.41x - 6.49y) \cdot 10^{-4} + 11.1$
Xmipp	$(-3.66x - 3.85y) \cdot 10^{-5} + 8.63$	$(-1.32x - 6.25y) \cdot 10^{-4} + 11.1$
CTFFIND3	$(-3.35x - 4.37y) \cdot 10^{-5} + 8.72$	$(-1.26x - 6.21y) \cdot 10^{-4} + 11.2$

Table 9
Processing times obtained by each micrograph of the P53 dataset when the different 64 submicrographs are processed locally by the different methods.

	Untilted$_1$ (s)	Tilted$_1$ (s)
FASTDEF	832	720
FASTDEF + Xmipp	1226	1102
Xmipp	6220	6012
CTFFIND3	18013	18240
	Untilted$_2$ (s)	Tilted$_2$ (s)
FASTDEF	867	751
FASTDEF + Xmipp	1899	1763
Xmipp	6422	5699
CTFFIND3	18211	17995

We have also obtained the CTF parameters of four micrographs taken in tilt pairs at tilt angles of 0° and 45° under low-dose conditions in a JEOL JEM-2200FS electron microscope and using the P53 dataset. Note that in this dataset, Xmipp, FASTDEF and CTFFIND3 methods obtain the local PSDs without periodogram averaging and using individual images of size 256 × 256 px. In Table 8 we show the plane parameters that best fit the locally retrieved defocus average values using the different methods. As can be seen from Table 8, there is a good agreement between the different plane fittings. Additionally, in Table 9 we show the processing times obtained when the different 64 submicrographs are processed by the different methods. As can be appreciated from Table 9, the FASTDEF and FASTDEF + Xmipp methods are significantly faster than the Xmipp and CTFFIND3 approaches. The processing times per micrograph are 12 ± 1 s, 23 ± 6 s, 95 ± 5 s and 283 ± 2 s, when we use FASTDEF and FASTDEF + Xmipp, Xmipp and CTFFIND3 methods, respectively. Note that these processing times have been obtained using a defocus search range of [0.5, 10] μm for both the Xmipp and CTFFIND3 methods, as in all the cases presented before.
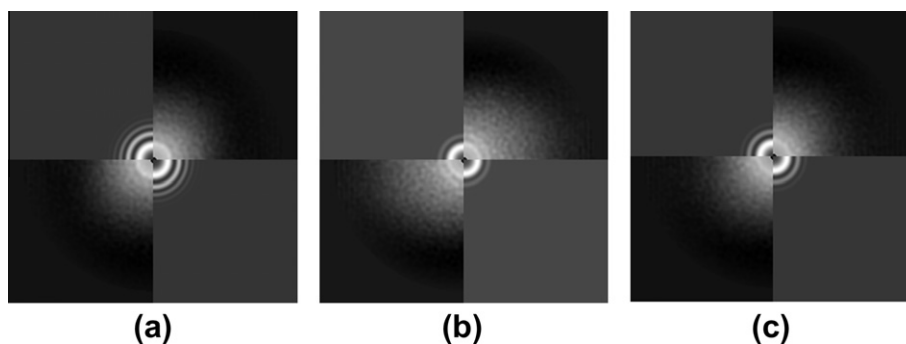
Finally, encouraged by the previous results, we have made a test using defocus series of three cryo-electron micrographs of Micropore© water alone on the cryo-EM grid. In this case the images where obtained with a JEOL 2100F electron microscope with an acceleration voltage of 200 kV, a spherical aberration of 0.5 mm, and a magnification of 50000×. Fig. 9 shows the enhanced experimental PSDs and the obtained PSDs using the FASTDEF + Xmipp method for the three micrographs. As can be seen from Fig. 9, the proposed method can recover the CTF parameters in these conditions.

4. Conclusions

In this work, we have presented a novel parameter-free approach to recover the CTF parameters (defocus and astigmatism) of a micrograph in a fast way without the need of non-linear optimization procedures and/or initial defocus estimations. Therefore, the proposed method is very suitable for High Throughput work. The obtained CTF parameters can be further refined by a posterior optimization, if desired. The proposed method is based on a fully non-parametric estimation approach as our method does not need any previous assumption about the CTF model. Additionally, it opens the way to well-defined extensions to the estimation of higher order aberrations. This approach considers the CTF as a fringe pattern where a two-dimensional phase, that contains the desired information about the microscope aberrations, is modulated by a sine function. Therefore, the objective phase can be obtained by a quadrature filter. We have tested the proposed method using simulated and experimental PSDs and we have compared the results with the results obtained by Xmipp and CTFFIND3 methods.

Appendix A

The wrapping operator $W[\cdot]$ transforms a continuous and smooth phase Φ, with a dynamic range larger than 2π rad, into a discontinuous phase with a limited dynamic range inside the range $(-\pi/2, \pi/2]$ rad as

Fig.9. Enhanced experimental and fitted PSDs using the FASTDEF + Xmipp method for micrographs with only ice (a), (b), (c).
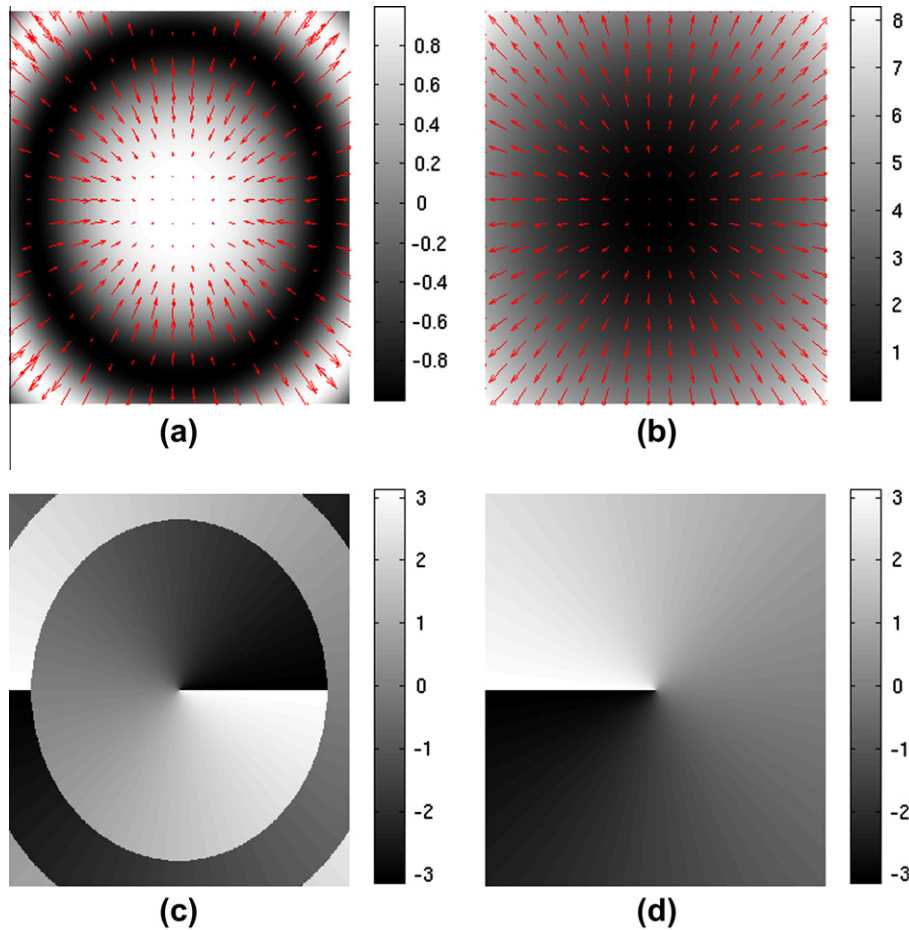
Fig.10. (Color online) Simulated enhanced PSD where the envelope function is equals to one in every pixel and corresponding gradient vectors (a), phase map $2\chi(\mathbf{R})$ and corresponding gradient vectors (b), orientation $\theta(\mathbf{R})$ (c) and phase direction $D(\mathbf{R})$ (d) maps.

$$W[\Phi(\mathbf{R})] = \Phi(\mathbf{R}) - 2\pi m \qquad (A1)$$

with m an integer number corresponding to

$$m = \text{INT}\left[\frac{\Phi(\mathbf{R})}{2\pi}\right] \qquad (A2)$$

and INT[·] is a function that maps a real number to the largest previous integer. Therefore, INT[x] is the largest integer not greater than x, being x an arbitrary real number.

Appendix B

The phase direction map, $D(\mathbf{R})$ corresponds to the subtended angle of the phase gradient vector with respect to the R_x-axis

$$D(\mathbf{R}) = \arctan\left(\frac{\nabla_{R_y}\chi(\mathbf{R})}{\nabla_{R_x}\chi(\mathbf{R})}\right) \qquad (B1)$$

where ∇_{R_x} and ∇_{R_y} corresponds to the derivatives along the R_x and R_y axes respectively. Obviously, we cannot obtain directly the phase direction map as the phase is indeed the quantity we want to retrieve. Instead of obtaining the direction map $D(\mathbf{R})$, we can compute the orientation map that corresponds to

$$\theta(\mathbf{R}) = \arctan\left(\frac{\nabla_{R_y}PSD_m}{\nabla_{R_x}PSD_m}\right) \qquad (B2)$$

with $\vec{\nabla}PSD_m(\mathbf{R}) = -2\sigma_{nb}^2 E^2(\mathbf{R})\sin(2\chi(\mathbf{R}) + 2\varphi)\vec{\nabla}\chi(\mathbf{R})$, where we have considered that the envelope function $E(\mathbf{R})$ is a low frequency signal. Observe that the arctangent function distinguishes between diametrically opposite directions. If in Eq. (B2) the numerator and

denominator have both positive sign, the resultant angle will be in the first quadrant. However, if they have both negative sign the angle will be in the fourth quadrant. Therefore, the relationship between the direction $D(\mathbf{R})$ and orientation $\theta(\mathbf{R})$ maps is given by

$$D(\mathbf{R}) = \begin{cases} \theta(\mathbf{R}) & \sin(2\chi(\mathbf{R}) + 2\phi) < 0 \\ \theta(\mathbf{R}) + \pi & \sin(2\chi(\mathbf{R}) + 2\phi) > 0 \end{cases} \qquad (B3)$$

We can solve this ambiguity problem and compute the phase direction map regularizing the orientation map imposing continuity (Villa et al., 2005). The method presented in (Villa et al., 2005) can obtain the direction from the orientation map in very complex fringe patterns. In order to clarify these concepts, we show in Fig. 10(a) set of images. Fig. 10(a) shows a simulated PSD after performing background suppression and mean subtraction whose mathematical expression is given in Expression (7). For simplicity, in Fig. 10(a) $\sigma_{nb}^2 E^2(\mathbf{R})$ is equal to one in every pixel. We overlay the corresponding gradient vectors $\nabla PSD_m(\mathbf{R})$ at some points. Fig. 10(b) shows the absolute phase map, $2\chi(\mathbf{R}) + 2\varphi$, and its corresponding gradient vectors, $\nabla(2\chi(\mathbf{R}))$, at different pixels. Additionally, in Fig. 10(c) and (d) we show the respective orientation $\theta(\mathbf{R})$ and direction $D(\mathbf{R})$ maps. As can be seen from Fig. 10, there is an ambiguity between $\theta(\mathbf{R})$ and $D(\mathbf{R})$ in some points caused by the sign changes introduced by the sine term in Eq. (B3).

Appendix C

In this section, we give a mathematical justification of Eq. (14). Note that if we assume that the CTF is not affected by astigmatism, the modulating phase is given by

$$\chi(\mathbf{R}) = \pi\lambda_{re}\left(-\Delta f_{avg}\left(R_x^2 + R_y^2\right) + \frac{C_s\left(R_x^2 + R_y^2\right)^2\lambda_{re}^2}{2}\right) \qquad (C1)$$

and the gradient components of $\chi(\mathbf{R})$ are

$$\nabla_{R_x}\chi(\mathbf{R}) = 2\pi\lambda_{re}R_x\left(-\Delta f_{avg} + C_s\left(R_x^2 + R_y^2\right)\lambda_{re}^2\right)$$
$$\nabla_{R_y}\chi(\mathbf{R}) = 2\pi\lambda_{re}R_y\left(-\Delta f_{avg} + C_s(R_x^2 + R_y^2)\lambda_{re}^2\right) \qquad (C2)$$

The direction phase map, defined in Eq. (11), corresponds to

$$D(\mathbf{R}) = \arctan\left(\frac{\nabla_{R_y}\chi(\mathbf{R})}{\nabla_{R_x}\chi(\mathbf{R})}\right) = \arctan\left(\frac{R_y}{R_x}\right) \qquad (C3)$$

The direction phase map can be obtained by Eq. (A.3) if the astigmatism is small compared with the defocus or spherical aberration components. Note that the error obtained in the modulating phase due to this approximation is quadratic with respect to the error in the determination of D. Suppose that we compute the phase direction from Eq. (A.3) in the presence of astigmatism so we obtain

$$\tilde{D}(\mathbf{R}) = D(\mathbf{R}) + \delta(\mathbf{R}) \qquad (C4)$$

where $D(\mathbf{R})$ and $\tilde{D}(\mathbf{R})$ are the actual and computed phase direction maps and $\delta(\mathbf{R}) \in [-\pi/2, \pi/2)$ (rad), is the error that is typically small because defocus is usually the dominant component of the modulating phase and then $\delta(\mathbf{R}) << 1$. The quasi-quadrature signal of the PSD_m is given from Expression (15)

$$\tilde{Q}[PSD_m(\mathbf{R})] = -i\exp\left(-i(D(\mathbf{R}) + \delta(\mathbf{R}))\right)SPHT[PSD_m(\mathbf{R})] \qquad (C5)$$

that can be rewritten in terms of the actual quadrature signal as

$$\tilde{Q}[PSD_m(\mathbf{R})] = \text{Re}[\exp(-i(\delta(\mathbf{R})))Q[PSD_m(\mathbf{R})]] \qquad (C6)$$

and

$$\tilde{Q}[PSD_m(\mathbf{R})] = \cos(\delta(\mathbf{R}))Q[PSD_m(\mathbf{R})] \qquad (C7)$$

where $\text{Re}[\cdot]$ is the real part. If $\delta(\mathbf{R}) << 1$ we can approximate

$$\tilde{Q}[PSD_m(\mathbf{R})] = \left(1 + \delta^2(\mathbf{R})\right)Q[PSD_m(\mathbf{R})] \qquad (C8)$$

And finally the modulating phase given by Eq. (16)

$$W[2\chi(\mathbf{R}) + 2\varphi] = \arctan\left(\frac{(1 + \delta^2(\mathbf{R}))Q[PSD_m(\mathbf{R})]}{PSD_m(\mathbf{R})}\right) \qquad (C9)$$

where it can be seen as mentioned before that the error is quadratic in $\delta^2(\mathbf{R})$.

Appendix D

In this section we introduce the mathematical description of the Zernike polynomials. There are even and odd Zernike polynomials. The even ones are defined as

$$ZPol_n^m(r, \alpha) = R_n^m(r)\cos(m\alpha) \qquad (D1)$$

and the odd ones are given by

$$ZPol_n^m(r, \alpha) = R_n^m(r)\sin(m\alpha) \qquad (D2)$$

with, r and α the radial and angular polar coordinates, m and n non negative integers such that $n \geqslant m$, θ the azimuthal angle and r the radial coordinate with $0 \leqslant r \leqslant 1$. The radial polynomials R_n^m are defined as

$$R_n^m(r) = \sum_{k=0}^{(n-m)/2} \frac{(-1)^k(n-k)!}{k!((n+m)/2 - k)!((n-m)/2 - k)!}r^{n-2k} \qquad (D3)$$

Typically, it is more convenient to use a Zernike representation that uses a single index instead of two. A conventional mapping of the two indices n and m to a single index j has been introduced by Noll (Noll, 1976) and consists in the following rule; even Zernike –with azimuthal part given by $\cos(m\alpha)$ and shown in Eq. (D1) –obtain even indices j, the odd ones obtain odd indices j and within a given n, lower values of m obtain lower j.

References

Avila-Sakar, A.J., Guan, T.L., Arad, T., Schmid, M.F., Loke, T.W., et al., 1994. Electron cryomicroscopy of bacillus stearothermophilus 50S ribosomal subunits crystallized on phospholipid monolayers. Journal of Molecular Biology 239, 689–697.

Born, M., Wolf, E., 1975. Principles of Optics, fifth ed. Pergamon Press, Oxford.

Fernández, J.J., Sanjurjo, J., Carazo, J.M., 1997. A spectral estimation approach to contrast transfer function detection in electron microscopy. Ultramicroscopy 68, 267–295.

Flynn, T.J., 1997. Two-dimensional phase unwrapping with minimum weighted discontinuity. Journal of the Optical Society of America A 14, 2692–2701.

Frank, J., 2002. Single-particle imaging of macromolecules by cryo-electron microscopy. Annual Review of Biophysics and Biomolecular Structure 31, 303–319.

Ghihlia, D.C., Romero, L.A., 1994. Robust two-dimensional weighted and unweighted phase unwrapping that uses fast transforms and iterative methods. Journal of the Optical Society of America A 11, 11107–11117.

Glaeser, R.M., Typke, D., Tiemeijer, P.C., Pulokas, J., Cheng, A., 2011. Review: precise beam-tilt alignment and collimation are required to minimize the phase error associated with coma in high-resolution cryo-em. Journal of Structural Biology 174 (1), 1–10.

Goldstein, R., Zebker, H., Werner, C., 1988. Satellite radar interferometry: two-dimensional phase unwrapping. Radio Science 23, 713–720.

Henderson, R., 2004. Realizing the potential of electron cryo-microscopy. Quarterly Reviews of biophysics 37, 3–13.

Huang, Z., Baldwin, P.R., Mullapudi, S., Penczek, P.A., 2003. Automated determination of parameters describing power spectra of micrograph images in electron microscopy. Journal of Structural Biology 144, 79–94.

Jonic, S., Sorzano, C.O.S., Cottevieille, M., Larquet, E., Boisset, N., 2007. A novel method for improvement of visualization of power spectra for sorting cryo-electron micrographs and their local areas. Journal of Structural Biology 157, 156–167.

Larkin, K.G., Bone, D.J., Oldfield, M.A., 2001. Natural demodulation of two-dimensional fringe patterns. I. General background of the spiral phase quadrature transform. Journal of the Optical Society of America A 18, 1862–1870.

Ludtke, S.J., Baldwin, P.R., Chiu, W., 1999. EMAN: semiautomated software for high-resolution single-particle reconstructions. Journal of Structural Biology 128, 82–97.

Mallick, S.P., Carragher, B., Potter, C.S., Kriegman, D.J., 2005. ACE: automated CTF estimation. Ultramicroscopy 104, 8–29.

Melero, R., Rajagopalan, S., Lázaro, M., Joerfer, A.C., et al., 2011. Electron microscopy studies on the quaternary structure of p53 reveal different binding modes for p53 tetramers in complex with DNA. Proceedings of the National Academy of Sciences of the United States of America 108, 557–562.

Mindell, J.A., Grigorieff, N., 2003. Accurate determination of local defocus and specimen tilt in electron microscopy. Journal of Structural Biology 142, 334–347.

MobileReference, 2009. Mathematical Tables Table of Derivatives (List of Differentiation Identities). MobileReference.

Navarro, M.A., Estrada, J.C., Servin, M., Quiroga, J.A., Vargas, J., 2012. Fast two-dimensional simultaneous phase unwrapping and low-pass filtering. Optics Express 20, 2556–2561.

Noll, R.J., 1976. Zernike polynomials and atmospheric turbulence. Journal of the Optical Society of America 66, 207–211.

Sander, B., Golas, M.M., Stark, H., 2003. Automatic CTF correction for single particles based upon multivariate statistical analysis of individual power spectra. Journal of Structural Biology 142, 392–401.

Sorzano, C.O.S., Marabini, R., Velázquez-Muriel, J., Bilbao-Castro, J.R., Scheres, S.H.W., Carazo, J.M., Pascual-Montano, A., 2004. XMIPP: a new generation of an open-source image processing package for Electron Microscopy. Journal of Structural Biology 148, 194–204.

Sorzano, C.O.S., Jonic, S., Núñez-Ramírez, R., Boisset, N., Carazo, J.M., 2007. Fast, robust, and accurate determination of transmission electron microscopy contrast transfer function. Journal of Structural Biology 160, 249–262.

Van Heel, M., Gowen, B., Matadeen, R., 2000. Single-particle electron cryo-microscopy: towards atomic resolution. Quarterly Reviews of Biophysics 33, 307–369.

Velázquez-Muriel, J.A., Sorzano, C.O.S., Fernández, J.J., Carazo, J.M., 2003. A method for estimating the CTF in electron microscopy based on ARMA models and parameter adjusting. Ultramicroscopy 96, 17–35.

Villa, J., De la Rosa, I., Miramontes, G., Quiroga, J.A., 2005. Phase recovery from a single pattern using an orientational vector-field-regularized estimator. Journal of the Optical Society of America A 22, 2766–2773.

Vulović, M., Franken, E., Ravelli, R.B., van Vliet, L.J., Rieger, B., 2012. Precise and unbiased estimation of astigmatism and defocus in transmission electron microscopy. Ultramicroscopy 116, 115–134.

Wolf, M., Garcea, R.L., Grigorieff, N., Harrison, S.C., 2010. Subunit interactions in bovine papillomavirus. Proceedings of the National Academy of Sciences of the United States of America 107, 6298–6303.

Wyant, J.C., Creath, K., 1992. Basic wavefront aberration theory for optical metrology. Applied Optics and Optical Engineering 11, 27–39.